J. Fluid Mech. (2013), *vol.* 727, *pp.* 509–532.
doi:10.1017/jfm.2013.285

The structure of sidewall boundary layers in confined rotating Rayleigh–Bénard convection

R. P. J. Kunnen[1,†], H. J. H. Clercx[1,2] and G. J. F. van Heijst[1]

[1]Fluid Dynamics Laboratory, Department of Applied Physics and J. M. Burgers Centre for Fluid Dynamics, Eindhoven University of Technology, P.O. Box 513, 5600 MB Eindhoven, The Netherlands

[2]Department of Applied Mathematics, University of Twente, P.O. Box 217, 7500 AE Enschede, The Netherlands

(Received 14 September 2012; revised 24 April 2013; accepted 29 May 2013; first published online 27 June 2013)

Turbulent rotating convection is usually studied in a cylindrical geometry, as this is its most convenient experimental realization. In our previous work (Kunnen *et al.*, *J. Fluid Mech.*, vol. 688, 2011, pp. 422–442) we studied turbulent rotating convection in a cylinder with the emphasis on the boundary layers. A secondary circulation with a convoluted spatial structure has been observed in mean velocity plots. Here we present a linear boundary-layer analysis of this flow, which leads to a model of the circulation. The model consists of two independent parts: an internal recirculation within the sidewall boundary layer, and a bulk-driven domain-filling circulation. Both contributions exhibit the typical structure of the Stewartson boundary layer near the sidewall: a sandwich structure of two boundary layers of typical thicknesses $E^{1/4}$ and $E^{1/3}$, where E is the Ekman number. Although the structure of the bulk-driven circulation may change considerably depending on the Ekman number, the boundary-layer recirculation is present at all Ekman numbers in the range $0.72 \times 10^{-5} \leqslant E \leqslant 5.76 \times 10^{-5}$ considered here.

Key words: Bénard convection, boundary layer structure, rotating flows

1. Introduction

In many geophysical and astrophysical flows, the interplay of buoyancy and the Coriolis force due to rotation of the celestial body is of eminent importance. Examples include deep oceanic convection (Marshall & Schott 1999) and the convective outer layer of the Sun (Miesch 2000). There are also specific technological applications where such conditions occur, for example, in chemical vapour deposition onto a rotating target (van Santen, Kleijn & van den Akker 2000).

This fundamental interaction of buoyancy and rotation is most conveniently studied in the simplified setting of rotating Rayleigh–Bénard (RRB) convection (Chandrasekhar 1961): a layer of fluid enclosed by parallel horizontal plates is heated from below, cooled from above and rotated about a vertical axis, aligned with the gravitational acceleration. Experimental investigations of the RRB system obviously have to introduce some lateral confinement. The preferred geometry for most experiments (Rossby 1969; Zhong, Ecke & Steinberg 1991, 1993; Ecke & Liu

† Email address for correspondence: r.p.j.kunnen@tue.nl

1998; Vorobieff & Ecke 1998*a*,*b*; Hart & Ohlsen 1999; Hart, Kittelman & Ohlsen 2002; Vorobieff & Ecke 2002; Kunnen, Clercx & Geurts 2008*a*,*b*; Zhong *et al.* 2009; Kunnen, Geurts & Clercx 2010*a*,*b*; Niemela, Babuin & Sreenivasan 2010; Weiss *et al.* 2010; Zhong & Ahlers 2010; Kunnen *et al.* 2011; Stevens *et al.* 2011; Weiss & Ahlers 2011*a*,*b*) is an upright cylinder. For comparison with those experiments, many direct numerical simulations in this geometry have been carried out (Kunnen *et al.* 2008*a*; Zhong *et al.* 2009; Kunnen *et al.* 2010*a*,*b*; Stevens, Clercx & Lohse 2010; Weiss *et al.* 2010; Kunnen *et al.* 2011; Stevens *et al.* 2011; Stevens, Clercx & Lohse 2012). The flow inside such a container can be described with four non-dimensional parameters. The Rayleigh number Ra and the Prandtl number σ are defined as in classical Rayleigh–Bénard convection problems,

$$Ra = \frac{g\alpha \Delta T H^3}{\nu\kappa}, \quad \sigma = \frac{\nu}{\kappa}, \tag{1.1}$$

where g represents the gravitational acceleration, H is the height of the fluid layer and ΔT is the imposed temperature difference between the bottom and top plates. The thermal expansion coefficient α, kinematic viscosity ν and thermal diffusivity κ are properties of the fluid. Furthermore, a dimensionless parameter must quantify the effects of rotation. In view of the boundary-layer analysis that follows, we introduce the Ekman number,

$$E = \frac{\nu}{\Omega H^2}, \tag{1.2}$$

with Ω the angular velocity. A final parameter is the diameter-to-height aspect ratio of the cylinder, $\Gamma = D/H$ (D is the diameter).

Our recent investigation (Kunnen *et al.* 2011) using direct numerical simulation (DNS) of this flow problem has revealed a remarkable boundary-layer structure in the averaged velocity and temperature fields. The azimuthally and temporally averaged velocity and temperature fields as presented in Kunnen *et al.* (2011) have been reproduced here; figure 1 depicts the entire extent of the cylinder. In these plots the left-hand side coincides with the cylinder axis and the right-hand side with the sidewall. Figure 2 shows an enlarged view of the corner region. Indeed, complex boundary-layer structures are observed near the bottom and top plates as well as adjacent to the sidewall. They are the so-called Ekman and Stewartson boundary layers (Greenspan 1968).

In this paper we describe these boundary layers with linear boundary-layer theory. We derive a linear flow field consisting of two independent contributions in § 2. The theoretical results are compared with the DNS solutions in § 3. In § 4 we conclude with some suggestions for further research.

2. Linear boundary-layer analysis

Consider an upright cylinder of height H and radius RH (R is the dimensionless radius) rotating at an angular velocity Ω about its vertical axis. It is filled with a Newtonian liquid that is set in motion by thermal effects. We adopt the Boussinesq approximation: the fluid properties ν, κ and α are constant, independent of temperature, and density variations are negligible except in the buoyancy term. The governing equations in a corotating frame of reference are (Chandrasekhar 1961)

$$\frac{\partial \boldsymbol{u}}{\partial t} + Ro(\boldsymbol{u}\cdot\nabla)\boldsymbol{u} + 2\hat{\boldsymbol{z}}\times\boldsymbol{u} = -\nabla p + E\nabla^2\boldsymbol{u} + RoT\hat{\boldsymbol{z}}, \tag{2.1a}$$

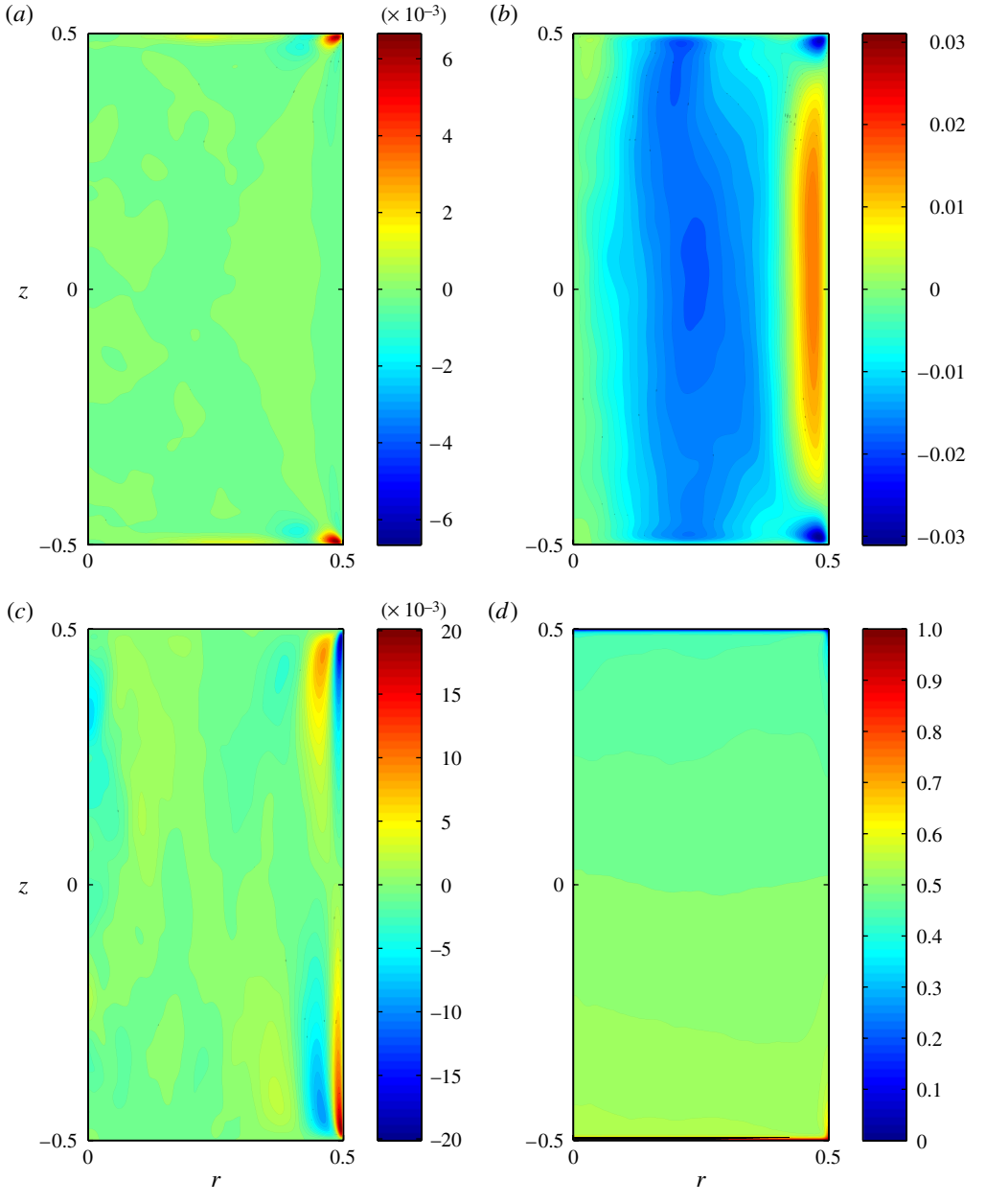

FIGURE 1. Temporal and azimuthal averages of velocity and temperature from a direct numerical simulation of turbulent rotating convection at $Ra = 1 \times 10^9$, $\sigma = 6.4$, $E = 5.76 \times 10^{-5}$ and $\Gamma = 1$. Included are (*a*) radial (u), (*b*) azimuthal (v) and (*c*) vertical (w) velocity components and (*d*) temperature (T). The left-hand side of each panel ($r = 0$) coincides with the cylinder axis; the right-hand side ($r = R = 0.5$) corresponds with the sidewall. Reproduced from Kunnen *et al.* (2011).

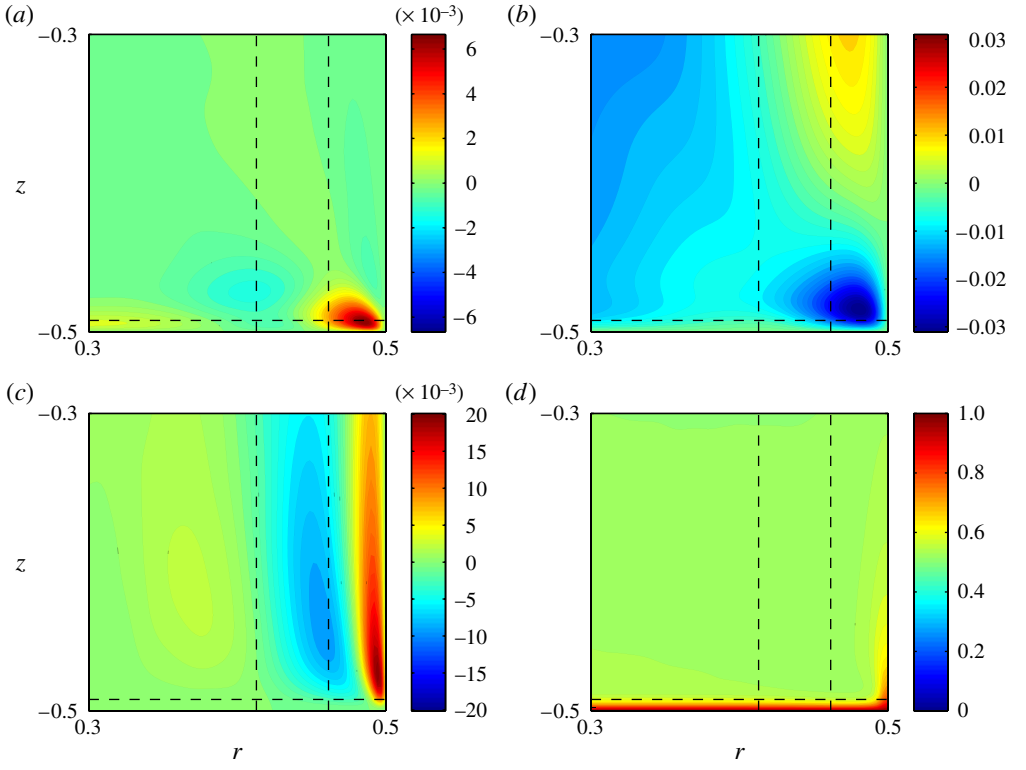

FIGURE 2. Close-up of the lower right-hand corner region of figure 1. The right-hand side of each panel ($r = R = 0.5$) corresponds with the sidewall. The dashed lines represent the boundary layer thicknesses $\delta_E = E^{1/2}$ near the bottom and top plates, $\delta_{S,1/3} = E^{1/3}$ closest to the sidewall, and $\delta_{S,1/4} = E^{1/4}$. Included are (*a*) radial (u), (*b*) azimuthal (v) and (*c*) vertical (w) velocity components and (*d*) temperature (T).

$$\boldsymbol{\nabla} \cdot \boldsymbol{u} = 0, \tag{2.1b}$$

$$\frac{\partial T}{\partial t} + Ro(\boldsymbol{u} \cdot \boldsymbol{\nabla})T = \frac{E}{\sigma}\nabla^2 T, \tag{2.1c}$$

which represent the evolution in time t (scaled with $1/\Omega$) of a dimensionless velocity $\boldsymbol{u} = (u, v, w)$ with its radial, azimuthal and vertical components, respectively (scaled by velocity scale $U = \sqrt{g\alpha\Delta TH}$) and dimensionless temperature T (scaled with ΔT). Vector $\hat{\boldsymbol{z}}$ is the vertical unit vector pointing upwards, parallel to the rotation vector. The length scale is H and the pressure is scaled with $\rho UH\Omega$ (ρ is the fluid density). Here the Rossby number $Ro = U/(\Omega H)$ is introduced. The Ekman number $E = \nu/(\Omega H^2)$ is a small parameter. The main assumptions of this analysis are: (i) viscous effects can be neglected except for in the regions close to the walls, where viscosity is essential to fulfil the no-slip conditions; (ii) there is a mean circulation pattern independent of time and azimuthal orientation; and (iii) it is a crucial assumption that the Rossby number $Ro = U/(\Omega H)$ is negligibly small, as otherwise the analytical approach is all but impossible given the nonlinearity of the Navier–Stokes equations (2.1*a*) and the heat equation (2.1*c*). This latter assumption leads to the linearized problem, a prerequisite that is all but required in order to obtain an analytical solution. A notable

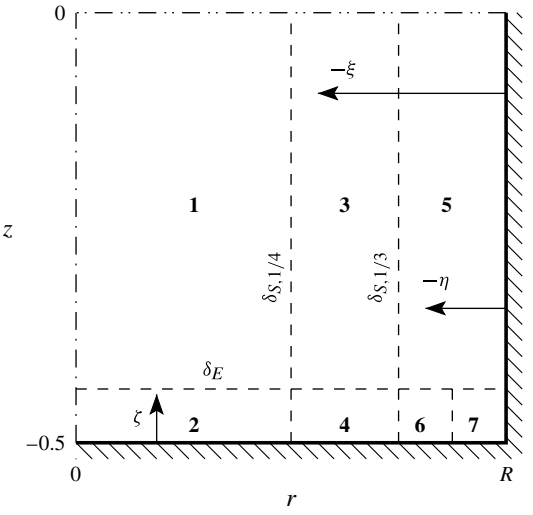

FIGURE 3. Sketch of the regions of the flow domain (bold numbers) with the bounding boundary-layer thicknesses δ_E, $\delta_{S,1/4}$ and $\delta_{S,1/3}$ (dashed lines; not to scale) and boundary-layer coordinates ζ, ξ and η to be introduced later. Only the lower half of the domain is included; the top half follows from symmetry.

side effect is that the buoyancy force $RoT\hat{\boldsymbol{z}}$, while being responsible for the fluid motion in the first place, actually drops out of the equation. Thermal effects determine the strength of the circulation, which is an undetermined free parameter in the model. It is assumed that the flow, although induced by buoyancy, has a phenomenology that is independent of the magnitude of the thermal forcing and is exclusively determined by the Ekman number E and the dimensionless radius R. This simplification will be validated by comparing the theoretical model with DNS results.

To describe the mean circulation pattern, we can thus consider the linearized, time and azimuthally averaged equations for this flow problem:

$$2\hat{\boldsymbol{z}} \times \boldsymbol{u} = -\boldsymbol{\nabla} p + E\nabla^2 \boldsymbol{u}, \tag{2.2a}$$

$$\boldsymbol{\nabla} \cdot \boldsymbol{u} = 0, \tag{2.2b}$$

where the viscous term $E\nabla^2\boldsymbol{u}$ only plays a role in the boundary-layer regions. The dimensionless coordinates are $0 \leqslant r \leqslant R$ for the radial direction and $-1/2 \leqslant z \leqslant 1/2$ for the vertical direction. By azimuthal averaging, the problem is independent of the azimuthal angle θ.

We can now distinguish the bulk region (away from the walls of the container) from the boundary-layer regions near the bottom and top plates, as well as near the sidewall. Only close to the walls does the viscous term contribute significantly to the equation of motion (2.2*a*) – outside the boundary layers, the flow is inviscid and in geostrophic balance. The solution of the flow problem is essentially an expansion with powers of the Ekman number E, which is a small parameter. Figure 3 presents a schematic view of the various regions of the flow domain considered here. The boundary layers on the horizontal plates are Ekman layers with characteristic thickness $\delta_E = E^{1/2}$. The Stewartson layer at the sidewall has a sandwich structure consisting of two nested layers, the inner of thickness $\delta_{S,1/3} = E^{1/3}$ and the outer of thickness $\delta_{S,1/4} = E^{1/4}$. The following flow regions can be distinguished: **1**, geostrophic bulk; **2**, Ekman layer; **3**,

Stewartson $E^{1/4}$ layer; **4**, Ekman extension of the Stewartson $E^{1/4}$ layer; **5**, Stewartson $E^{1/3}$ layer; **6**, Ekman extension of the Stewartson $E^{1/3}$ layer; and **7**, corner region of size $E^{1/2} \times E^{1/2}$ where the Ekman-layer dynamics is no longer dominant. In the next paragraphs these regions will be explained further.

The solution procedure presented in the following sections provides individual contributions to the total velocity field $\boldsymbol{u} = (u, v, w)$. Each individual contribution to the total field need not fulfil the boundary conditions. Instead, each boundary-layer contribution *corrects* another field at a boundary so that the sum of velocities fulfils the boundary condition and/or carries a flux to preserve incompressibility. All of the boundary-layer correction contributions rapidly drop off to zero outside of their designated boundary layers. This method has been applied before by Barcilon & Pedlosky (1967*a*,*b*). Another way of presenting the results would be a *matching* approach, where velocities are matched on the edges of boundary layers (e.g. at $z = -1/2 + \delta_E$, where δ_E is the thickness of the Ekman boundary layer). We have chosen to apply the correction method for three reasons. (i) It better reveals the origin of the new boundary-layer circulation, in the derivation of which we explicitly make use of the freedom of having non-zero velocities on the sidewall, later to be compensated by a correction velocity field. (ii) The numerical evaluation is more convenient. The total velocity field is just a sum of all the individual contributions; there is no need to divide the domain into parts where some contributions are present or absent. (iii) The default treatment of the $E^{1/3}$ layer is to serve as a *correction* field for the velocity field in the $E^{1/4}$ layer, which cannot satisfy the boundary conditions by itself (e.g. Greenspan & Howard 1963; van Heijst 1986). The correction approach can be consistently applied throughout the analysis, whereas the matching approach is not possible there.

2.1. *Bulk-driven circulation*

An interesting feature in the visualization in figure 1 is the mean azimuthal velocity, which has a negative value in most of the domain. The assumption that the mean azimuthal velocity is linearly dependent on the radial coordinate r leads to a problem related to impulsive linear spin-up (Greenspan & Howard 1963; Benton & Clark 1974; Duck & Foster 2001). The findings are summarized in appendix A. This spin-up circulation is not enough for the complete description of the mean flow pattern. There is an independent boundary-layer recirculation that also contributes.

2.2. *Boundary-layer recirculation*

Figure 2 reveals a remarkable updraft emanating from the lower corner region. By symmetry, there is also a downdraft from the top corner; see figure 1. For the remainder of this paragraph, we shall mostly consider the bottom half of the domain; the top half follows from the symmetry. Note that the spin-up circulation of appendix A does not account for the updraft. The mean temperature field reveals that the updraft consists of hot fluid; it is therefore likely to be driven by buoyancy. Again, just as in the derivation of the linearized equations of motion, the assumption is made that buoyancy accounts for the *strength* of the circulation but not its *shape*; the buoyancy force is not included in these equations that determine the phenomenology of the circulation. To describe the updraft, we resort to the boundary-layer approximation of (2.2) with the assumption that radial derivatives are much larger than vertical derivatives. We also neglect curvature terms (valid when the boundary-layer thickness $\delta \ll R$) and arrive at the following set of equations for radial

velocity u, azimuthal velocity v, vertical velocity w and pressure p:

$$-2v = -\partial_r p + E\partial_r^2 u, \tag{2.3a}$$

$$2u = E\partial_r^2 v, \tag{2.3b}$$

$$0 = -\partial_z p + E\partial_r^2 w, \tag{2.3c}$$

$$\partial_r u + \partial_z w = 0, \tag{2.3d}$$

where we have introduced the notation $\partial_r = \partial/\partial r$, $\partial_r^n = \partial^n/\partial r^n$ for convenience. From similar problems of sidewall boundary layers (Stewartson 1957; Greenspan & Howard 1963; van Heijst 1983, 1986), we expect a nested two-layer structure with characteristic thicknesses $\delta_{S,1/3} = E^{1/3}$ and $\delta_{S,1/4} = E^{1/4}$ (regions **3** and **5** in figure 3, respectively). This structure is generally referred to as the Stewartson layer. In the following, we apply a similar analysis as in van Heijst (1983, 1986), who also considered Stewartson layers. We use a similar notation here; some more details of the procedure (albeit applied to different flow problems) can be found there.

For the thicker of the two layers, the Stewartson $E^{1/4}$ layer (region **3** in figure 3), the boundary-layer coordinate $\xi = (r - R)E^{-1/4}$ is introduced, which is negative inside the fluid. An order-of-magnitude analysis reveals that, when the azimuthal velocity component v is of order E^0, the radial component u must be of order $E^{1/2}$ as per (2.3*b*). By (2.3*d*) the vertical component w must be of order $E^{1/4}$. These equations have leading-order solutions of the form $u \sim E^{1/2}\exp(\sqrt{2}\xi)$, $v \sim E^0\exp(\sqrt{2}\xi)$, $w \sim E^{1/4}z\exp(\sqrt{2}\xi)$. From these functional forms, it can be inferred that this boundary layer cannot account for the updraft near the sidewall, given that the updraft is highly localized and is not accurately represented by a radial dependence of the form $\exp(\sqrt{2}\xi)$.

The updraft must thus be represented by the Stewartson $E^{1/3}$ layer (region **5** in figure 3). The analysis of this layer also starts at the boundary-layer equations (2.3). As the thickness of this boundary layer is $\delta_{S,1/3} = E^{1/3}$ (Proudman 1956; Stewartson 1957; Moore & Saffman 1969; van Heijst 1983, 1986), we define the boundary-layer coordinate as $\eta = (r - R)E^{-1/3}$. For the velocity and pressure, we now introduce a general expansion that will be useful later. Because of powers of E with exponents $1/4$, $1/3$ and $1/2$ occurring in this problem, an expansion in terms of $E^{1/12}$ is natural (Greenspan 1968):

$$(u, v, w, p) = \sum_{k=0}^{\infty} (E^{4/12}\tilde{u}_{(k)}, \tilde{v}_{(k)}, \tilde{w}_{(k)}, E^{4/12}\tilde{p}_{(k)})E^{k/12}. \tag{2.4}$$

After insertion of the expansion (2.4) into (2.3) we gather terms of equal powers of E. This leads to

$$-2\tilde{v}_{(k)} = -\partial_\eta \tilde{p}_{(k)}, \tag{2.5a}$$

$$2\tilde{u}_{(k)} = \partial_\eta^2 \tilde{v}_{(k)}, \tag{2.5b}$$

$$0 = -\partial_z \tilde{p}_{(k)} + \partial_\eta^2 \tilde{w}_{(k)}, \tag{2.5c}$$

$$\partial_\eta \tilde{u}_{(k)} + \partial_z \tilde{w}_{(k)} = 0, \tag{2.5d}$$

which is valid for $k = 0, 1, 2, 3$.

Close to the bottom and top plates the situation is different. Ekman layers are expected there (Greenspan 1968). Given that $\delta_E = E^{1/2} \ll \delta_{S,1/3} = E^{1/3}$, the Laplacian operator ∇^2 must be dominated by the vertical derivatives close to the plates (region **6**

in figure 3). The well-known Ekman solutions for the velocity field are expected there. In particular, the Ekman suction condition holds (Greenspan 1968). In this case $\tilde{w}_{(k+2)}$ and $\tilde{v}_{(k)}$ are coupled (van Heijst 1983):

$$\tilde{w}_{(k+2)}(z=\pm\tfrac{1}{2}) = \mp\tfrac{1}{2}\partial_\eta \tilde{v}_{(k)}(z=\pm\tfrac{1}{2}). \tag{2.6}$$

The Ekman suction condition (2.6) is valid in the $E^{1/3}$ layer up to a radial distance of $O(E^{1/2})$ from the sidewall. It is clear that, if we do not wish to consider negative powers of E, the Ekman condition couples the vertical velocity $\tilde{w}_{(2)}$ at $z=\pm 1/2$ to an azimuthal velocity $\tilde{v}_{(0)}$. Though generally absent, the $k=0$ field can be of importance in Stewartson layers, as in the case discussed by van Heijst (1983). The secondary circulation within the boundary layers that is introduced in what follows is a new, independent set of solutions that has not yet been reported in the literature.

The localized updraft emanating from the position where the bottom plate and the sidewall meet is a known flow structure also occurring when the plate and sidewall exhibit different rotation rates (Moore & Saffman 1969; van Heijst 1986). The updraft originates from the corner region (region **7** of figure 3), a region of typical dimensions $E^{1/2}\times E^{1/2}$, where the Ekman dynamics finally ceases to dominate. The flow from the corner region into the $E^{1/3}$ layer has a radial extent of typical size $E^{1/2}$, which is much smaller than the thickness $\delta_{S,1/3}=E^{1/3}$ of the $E^{1/3}$ layer. The upward vertical flow from the corner region can thus be mathematically treated as a singular influx into the $E^{1/3}$ layer at $\eta=0$ (Moore & Saffman 1969). Following Moore & Saffman (1969), we write in accordance with the Ekman condition (2.6) that $\tilde{w}_{(2)}(z=\pm 1/2)\sim\delta(\eta)$ and $\tilde{v}_{(0)}(z=\pm 1/2)\sim H(\eta)$, with $\delta(\eta)$ the Dirac delta function peaking at $\eta=0$ and $H(\eta)$ the Heaviside step function, which takes the values zero for $\eta<0$ and one for $\eta>0$. Furthermore, $\delta(\eta)=\partial_\eta H(\eta)$, so $\tilde{v}_{(0)}$ must thus 'step' from zero on the bottom and top plates to a finite value on the sidewall. We derive a $k=0$ field for which on the sidewall $\tilde{v}_{(0)}(\eta=0)=C$. Here C is a free parameter, which is essentially the amplitude of the boundary-layer recirculation; we will use it to match the theory to the DNS results. Obviously the boundary conditions for v as a whole are not satisfied; an additional contribution is still necessary. There are two candidates of the right order in E that could correct $\tilde{v}_{(0)}$ on the sidewall. The first, the bulk azimuthal velocity, cannot provide the correction. As summarized in appendix A, the bulk flow is coupled to a closed circulation; any extra azimuthal velocity would lead exclusively to an increased flux of the closed circulation. The second is the azimuthal component of the Stewartson $E^{1/4}$ layer (region **3** in figure 3). Owing to the quasi-geostrophic nature of the $E^{1/4}$ layer (the azimuthal velocity V being independent of z), we can conclude that $\tilde{v}_{(0)}$ on the sidewall must be independent of z as well for it to be corrected on the sidewall.

The general solution of (2.5) is obtained with standard methods, taking into account the vertical symmetries, and can be written as

$$\tilde{u}_{(k)} = -\frac{1}{2}\sum_{n=1}^{\infty}\gamma_n^2\cos(2\pi nz)[a_n\mathrm{e}^{\gamma_n\eta} - \omega^2 b_n\mathrm{e}^{-\omega\gamma_n\eta} - \omega c_n\mathrm{e}^{-\omega^2\gamma_n\eta}], \tag{2.7a}$$

$$\tilde{v}_{(k)} = -\sum_{n=1}^{\infty}\cos(2\pi nz)[a_n\mathrm{e}^{\gamma_n\eta} - b_n\mathrm{e}^{-\omega\gamma_n\eta} - c_n\mathrm{e}^{-\omega^2\gamma_n\eta}], \tag{2.7b}$$

$$\tilde{w}_{(k)} = \sum_{n=1}^{\infty}\sin(2\pi nz)[a_n\mathrm{e}^{\gamma_n\eta} + b_n\mathrm{e}^{-\omega\gamma_n\eta} + c_n\mathrm{e}^{-\omega^2\gamma_n\eta}], \tag{2.7c}$$

with the convenient notation $\gamma_n = (4\pi n)^{1/3}$ and $\omega = -1/2 + \mathrm{i}\sqrt{3}/2$. The coefficients a_n, b_n and c_n are to be determined using the boundary conditions. We require the solutions for $k = 0$. The boundary conditions are: $\tilde{u}_{(0)} = \tilde{v}_{(0)} = \tilde{w}_{(0)} = 0$ as $\eta \to -\infty$, and $\tilde{u}_{(0)} = \tilde{w}_{(0)} = 0$, $\tilde{v}_{(0)} = C$ for $\eta = 0$. We rewrite this latter boundary condition as a Fourier series using

$$\sum_{n=1}^{\infty} (-1)^n \cos(2\pi n z) = -\frac{1}{2} \tag{2.8}$$

(see e.g. Lighthill 1968). Application of these boundary conditions leads to

$$\left.\begin{aligned} a_n + b_n + c_n &= 0, \\ a_n - b_n - c_n &= 2C(-1)^n, \\ a_n - \omega^2 b_n - \omega c_n &= 0, \end{aligned}\right\} \tag{2.9}$$

resulting in

$$\left.\begin{aligned} a_n &= C(-1)^n, \\ b_n &= -\tfrac{1}{2}C(-1)^n(1 - \tfrac{1}{3}\mathrm{i}\sqrt{3}), \\ c_n &= -\tfrac{1}{2}C(-1)^n(1 + \tfrac{1}{3}\mathrm{i}\sqrt{3}). \end{aligned}\right\} \tag{2.10}$$

We thus arrive at the following solutions for the $k = 0$ field of the Stewartson $E^{1/3}$ layer (region **5** in figure 3):

$$\tilde{u}_{(0)} = -\frac{C}{2}\sum_{n=1}^{\infty} (-1)^n \gamma_n^2 \cos(2\pi n z) \times \left[\mathrm{e}^{\gamma_n \eta} - \mathrm{e}^{\gamma_n \eta/2}\left\{\cos\left(\frac{1}{2}\sqrt{3}\gamma_n\eta\right) + \frac{1}{\sqrt{3}}\sin\left(\frac{1}{2}\sqrt{3}\gamma_n\eta\right)\right\}\right], \tag{2.11a}$$

$$\tilde{v}_{(0)} = -C\sum_{n=1}^{\infty} (-1)^n \cos(2\pi n z) \times \left[\mathrm{e}^{\gamma_n \eta} + \mathrm{e}^{\gamma_n \eta/2}\left\{\cos\left(\frac{1}{2}\sqrt{3}\gamma_n\eta\right) - \frac{1}{\sqrt{3}}\sin\left(\frac{1}{2}\sqrt{3}\gamma_n\eta\right)\right\}\right], \tag{2.11b}$$

$$\tilde{w}_{(0)} = C\sum_{n=1}^{\infty} (-1)^n \sin(2\pi n z) \times \left[\mathrm{e}^{\gamma_n \eta} - \mathrm{e}^{\gamma_n \eta/2}\left\{\cos\left(\frac{1}{2}\sqrt{3}\gamma_n\eta\right) - \frac{1}{\sqrt{3}}\sin\left(\frac{1}{2}\sqrt{3}\gamma_n\eta\right)\right\}\right]. \tag{2.11c}$$

Although this field has an $O(E^0)$ contribution to the vertical velocity, the net vertical flux integrated over the boundary layer remains zero; it is an internal recirculation. In magnitude the flux is $O(E^{1/3})$, which is the leading-order contribution for this flow problem. The $k = 0$ field is the dominant contribution to the velocity field near the sidewall. The numerical evaluation of series like these is not straightforward; in appendix B we discuss this matter in more detail.

The $k = 0$ field is coupled to the bottom and top plates by Ekman layers that satisfy the Ekman condition (2.6). Since the Heaviside function $H(\eta)$ behaves as $H(\eta = 0) = 1/2$, we can write $\tilde{v}_{(0)}(z = \pm 1/2) = \mp 2CH(\eta)$. This implies that $\tilde{w}_{(2)}(z = \pm 1/2) = \mp C\delta(\eta)$; see (2.6). The flux carried by this vertical velocity is,

at $z=-1/2$,

$$Q\left(z=-\frac{1}{2}\right)=\int_{\delta_{S,1/3}} w\,\mathrm{d}r=\int_{-\infty}^{0}\tilde{w}_{(2)}E^{1/6}E^{1/3}\,\mathrm{d}\eta=CE^{1/2}\int_{-\infty}^{0}\delta(\eta)\,\mathrm{d}\eta=\frac{1}{2}CE^{1/2}. \tag{2.12}$$

By symmetry, at $z=0$ the flux must be reduced to zero. For the vertical dependence we take

$$Q(z)=-CzE^{1/2}. \tag{2.13}$$

One additional point to mention here is that equations (2.7) do not allow all three velocity components to be zero on the sidewall, as this would immediately lead to the coefficients a_n, b_n and c_n being identically zero. Here, $\tilde{u}_{(2)}$ can be non-zero on the sidewall, which will be compensated by the Stewartson $E^{1/4}$ layer that also compensates $\tilde{v}_{(0)}$ there. It is due to the required compensation by the $E^{1/4}$ layer that the linear z dependence of the flux is chosen; it corresponds to a radial velocity component that is independent of z, as is required of the radial velocity component in the $E^{1/4}$ layer.

Making $\tilde{v}_{(2)}$ and $\tilde{w}_{(2)}$ zero at $\eta=0$ gives $a_n=0$ and $b_n=-c_n$. These latter unknowns are fixed by the flux condition (2.13). From

$$\tilde{w}_{(2)}=\sum_{n=1}^{\infty}\sin(2\pi nz)[b_n\mathrm{e}^{-\omega\gamma_n\eta}-b_n\mathrm{e}^{-\omega^2\gamma_n\eta}], \tag{2.14}$$

the vertical flux is found to be

$$\begin{aligned}Q(z)&=\int_{\delta_{S,1/3}} w\,\mathrm{d}r=\int_{-\infty}^{0}\tilde{w}_{(2)}E^{1/6}E^{1/3}\,\mathrm{d}\eta\\&=E^{1/2}\sum_{n=1}^{\infty}b_n\sin(2\pi nz)\int_{-\infty}^{0}[\mathrm{e}^{-\omega\gamma_n\eta}-\mathrm{e}^{-\omega^2\gamma_n\eta}]\,\mathrm{d}\eta\\&=E^{1/2}\sum_{n=1}^{\infty}b_n\sin(2\pi nz)\frac{\mathrm{i}\sqrt{3}}{\gamma_n},\end{aligned} \tag{2.15}$$

which must be equal to (2.13), for which we can write (see Lighthill 1968)

$$Q(z)=-CzE^{1/2}=CE^{1/2}\sum_{n=1}^{\infty}\frac{(-1)^n}{n\pi}\sin(2\pi nz). \tag{2.16}$$

Hence,

$$b_n=C\frac{\gamma_n}{\mathrm{i}\sqrt{3}}\frac{(-1)^n}{n\pi}, \tag{2.17}$$

and the solutions for the $k=2$ field of the Stewartson $E^{1/3}$ layer (region **5** in figure 3) are

$$\tilde{u}_{(2)}=\frac{2C}{\sqrt{3}}\sum_{n=1}^{\infty}(-1)^n\cos(2\pi nz)\mathrm{e}^{\gamma_n\eta/2}\left[\sin\left(\frac{1}{2}\sqrt{3}\gamma_n\eta\right)-\sqrt{3}\cos\left(\frac{1}{2}\sqrt{3}\gamma_n\eta\right)\right], \tag{2.18a}$$

$$\tilde{v}_{(2)}=-\frac{8C}{\sqrt{3}}\sum_{n=1}^{\infty}\frac{(-1)^n}{\gamma_n^2}\cos(2\pi nz)\mathrm{e}^{\gamma_n\eta/2}\sin\left(\frac{1}{2}\sqrt{3}\gamma_n\eta\right), \tag{2.18b}$$

$$\tilde{w}_{(2)} = -\frac{8C}{\sqrt{3}} \sum_{n=1}^{\infty} \frac{(-1)^n}{\gamma_n^2} \sin(2\pi n z) \mathrm{e}^{\gamma_n \eta/2} \sin\left(\frac{1}{2}\sqrt{3}\gamma_n \eta\right). \tag{2.18c}$$

What remains now is to compensate $\tilde{v}_{(0)}(\eta = 0) = C$ and

$$\tilde{u}_{(2)}(\eta = 0) = -2CE^{1/2} \sum_{n=1}^{\infty} (-1)^n \cos(2\pi n z) = CE^{1/2}. \tag{2.19}$$

This is accomplished by a Stewartson $E^{1/4}$ layer (region **3** in figure 3) similar to that of the spin-up circulation of appendix A, but with different multiplicative constants:

$$U = -C \exp(\sqrt{2}\xi) E^{1/2}, \tag{2.20a}$$

$$V = -C \exp(\sqrt{2}\xi), \tag{2.20b}$$

$$W = \sqrt{2} C z \exp(\sqrt{2}\xi) E^{1/4}. \tag{2.20c}$$

In terms of boundary conditions on the sidewall, it is now satisfied that $U(\xi = 0) + \tilde{u}_{(2)}(\eta = 0)E^{1/2} = 0$ and $V(\xi = 0) + \tilde{v}_{(0)}(\eta = 0) = 0$. The corresponding Ekman-layer contributions (region **6** in figure 3) are

$$U_E = C \exp(\sqrt{2}\xi) \sin\zeta \, \mathrm{e}^{-\zeta}, \tag{2.21a}$$

$$V_E = C \exp(\sqrt{2}\xi) \cos\zeta \, \mathrm{e}^{-\zeta}, \tag{2.21b}$$

$$W_E = \tfrac{1}{2}\sqrt{2} C \exp(\sqrt{2}\xi)(\sin\zeta + \cos\zeta)\mathrm{e}^{-\zeta} E^{1/4}, \tag{2.21c}$$

which account for matching to the bottom plate: $U + U_E(\zeta = 0) = 0$, $V + V_E(\zeta = 0) = 0$ to leading order E^0, and $W(z = -1/2) + W_E(\zeta = 0) = 0$. This boundary layer has an uncompensated vertical velocity $W(\xi = 0)$ of order $E^{1/4}$, which necessitates a $k = 3$ contribution in the $E^{1/3}$ layer, denoted here with $(\tilde{u}_{(3)}, \tilde{v}_{(3)}, \tilde{w}_{(3)})$. The vertical velocity $\tilde{w}_{(3)}$ must be zero on the plates at $z = \pm 1/2$: the Ekman suction condition (2.6) should be met and a non-zero $\tilde{w}_{(3)}(z = \pm 1/2)$ would imply a non-zero $k = 1$ field. The resulting equations can be solved with standard methods and the solution for $\tilde{w}_{(3)}$ is expressed as a cosine series to guarantee that $\tilde{w}_{(3)}(z = \pm 1/2) = 0$. Also, $\tilde{u}_{(3)}$ and $\tilde{v}_{(3)}$ are zero on the horizontal plates and on the sidewall. In terms of the boundary-layer coordinate $\eta = (r - R)E^{-1/3}$, the $k = 3$ solutions of the Stewartson $E^{1/3}$ layer (region **5** in figure 3) are

$$\tilde{u}_{(3)} = -\sqrt{2} C \sum_{n=1}^{\infty} \frac{(-1)^n}{\gamma_n} \cos(2\pi n z) \times \left[\mathrm{e}^{\gamma_n \eta} - \mathrm{e}^{\gamma_n \eta/2} \left\{\cos\left(\frac{1}{2}\sqrt{3}\gamma_n \eta\right) - \sqrt{3}\sin\left(\frac{1}{2}\sqrt{3}\gamma_n \eta\right)\right\}\right], \tag{2.22a}$$

$$\tilde{v}_{(3)} = -\sqrt{2} C \sum_{n=1}^{\infty} \frac{(-1)^n}{2\pi n} \cos(2\pi n z) \times \left[\mathrm{e}^{\gamma_n \eta} - \mathrm{e}^{\gamma_n \eta/2} \left\{\cos\left(\frac{1}{2}\sqrt{3}\gamma_n \eta\right) + \sqrt{3}\sin\left(\frac{1}{2}\sqrt{3}\gamma_n \eta\right)\right\}\right], \tag{2.22b}$$

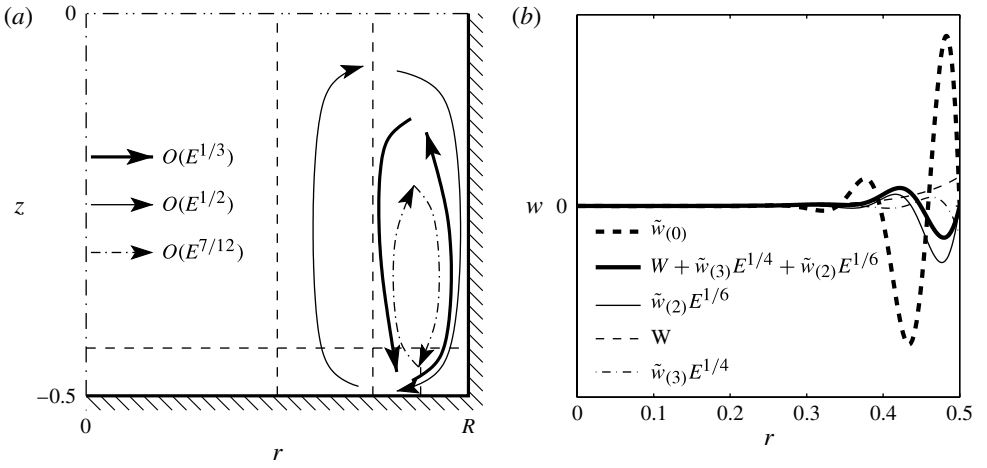

FIGURE 4. (*a*) Schematic view of the boundary-layer circulation driven by buoyancy near the sidewall. The thick solid arrows indicate the $O(E^{1/3})$ internal recirculation due to $\tilde{w}_{(0)}$. The thin solid arrows represent $O(E^{1/2})$ fluxes. The dash-dotted arrows indicate the $O(E^{7/12})$ recirculation. (*b*) Contributions to the vertical velocity of the boundary-layer circulation evaluated at height $z = -0.25$.

$$\tilde{w}_{(3)} = \sqrt{2}C \sum_{n=1}^{\infty} \frac{(-1)^n}{2\pi n} \sin(2\pi n z) \times \left[e^{\gamma_n \eta} + e^{\gamma_n \eta/2} \left\{ \cos\left(\frac{1}{2}\sqrt{3}\gamma_n \eta\right) + \sqrt{3}\sin\left(\frac{1}{2}\sqrt{3}\gamma_n \eta\right) \right\} \right]. \quad (2.22c)$$

Note that, with the Fourier series expansion (e.g. Lighthill 1968)

$$\sum_{n=1}^{\infty} \frac{(-1)^n}{\pi n} \sin(2\pi n z) = z, \quad (2.23)$$

we can conclude that, on the sidewall, $W(\xi = 0) + \tilde{w}_{(3)}(\eta = 0)E^{1/4} = 0$. Also, $\tilde{u}_{(3)}$ and $\tilde{v}_{(3)}$ are zero on the bottom and top plates as well as on the sidewall. Flux calculations of the $k = 3$ velocities reveal that the net radial and vertical fluxes are zero. Apparently, this velocity field provides no net transport, just an internal recirculation with an $O(E^{7/12})$ flux.

The boundary-layer circulation is sketched in figure 4(*a*). The largest contribution is the $k = 0$ velocity field in the $E^{1/3}$ layer, carrying an internal recirculation of $O(E^{1/3})$ (thick solid arrows). The thin solid arrows indicate the $O(E^{1/2})$ circulation carried by the $k = 2$ field in the $E^{1/3}$ layer and (U, V, W) in the $E^{1/4}$ layer, while the dash-dotted arrows represent the $O(E^{7/12})$ internal recirculation of the $k = 3$ field in the $E^{1/3}$ layer. The relative contributions to the vertical velocity w at $z = -0.25$ as a function of r are shown in figure 4(*b*). The $O(E^{1/3})$ internal recirculation is carried by $\tilde{w}_{(0)}$ (thick dashed line). The upward $O(E^{1/2})$ flux is due to W (thin dashed line) in the $E^{1/4}$ layer; the corresponding downward flux is due to $\tilde{w}_{(2)}$ in the $E^{1/3}$ layer (thin solid line). The boundary condition on the sidewall is met due to the additional $\tilde{w}_{(3)}$ contribution (thin dash-dotted line), carrying the $O(E^{7/12})$ recirculation. The sum $W + \tilde{w}_{(2)}E^{1/6} + \tilde{w}_{(3)}E^{1/4}$ (thick solid line) satisfies the no-slip boundary condition on the sidewall and carries

no net vertical flux. In both panels, a negative C is assumed, which is found from the comparison with the DNS results in § 3.

To complete the description of this circulation, one should consider the flow inside region **7** of figure 3, the corner region close to $r = R$, $z = \pm 1/2$. It has typical vertical and radial dimensions $E^{1/2} \times E^{1/2}$. In this region the leading-order equations have a different structure from those of the Ekman layers. The equations lead to a sixth-order partial differential equation in both radial and vertical boundary-layer coordinates, for which no simple solutions are available (Greenspan & Howard 1963). The solutions can be described implicitly by a flux argument: the radially outward flux from the Ekman extension of the $E^{1/4}$ layer associated with U_E, see (2.21*a*), is diverted upwards as a singular eruption into the $E^{1/3}$ layer, in the form of a $\delta(\eta)$ behaviour in $\tilde{w}_{(2)}(z = -1/2)$, see (2.18*c*). An explicit treatment of the velocity field in the corner region, even numerically, is not possible: although velocity profiles for the inflow through the Ekman layers are readily available to serve as boundary conditions, the corresponding outflow profiles as a function of the radial coordinate are unknown. However, given that the contributions of the corner region drop off rapidly as the distance to the walls becomes larger, our current analytical description is complete for most of the flow domain.

Thus we have arrived at a set of equations that, up to order $E^{1/4}$, gives a closed description of two independent circulations, one driven by anticyclonic vorticity in the bulk, the other by buoyancy adjacent to the sidewall. The velocity fields are summarized in table 1.

3. Comparison and discussion

The theoretical model needs to be validated with the DNS results. In § 3.1 we consider in detail the case $E = 5.76 \times 10^{-5}$, which is taken as an example from our earlier DNS and is shown in figures 1 and 2. We treat the dependence on the Ekman number in § 3.2.

3.1. *Comparison at* $E = 5.76 \times 10^{-5}$

The linear boundary-layer analysis has provided two independent contributions, the sum of which is to be compared with the DNS results. We have applied the following procedure.

Given that the numerical evaluation of the series expansions is cumbersome, especially near the endplates, the fit is conducted in the radial rather than the vertical direction. For independent fitting of the amplitudes C and C' of the boundary-layer and bulk circulations, respectively, it is best to revert to the vertical velocity component w: the boundary-layer circulation has a strong contribution of order E^0, while the bulk circulation contributes to order $E^{1/4}$ at most. Contributions to both u and v are to the same order in E for the two circulations. Furthermore, we restrict ourselves to the height $z = -0.25$ for the fit: it is the middle ground between $z = 0$ where $w = 0$ by symmetry and $z = -0.5$ where the description is incomplete as the contribution of the corner region is absent.

In the first step, the sum $w_{BL} = \tilde{w}_{(0)} + \tilde{w}_{(2)}E^{1/6} + W + \tilde{w}_{(3)}E^{1/4}$ of the vertical-velocity contributions that make up the boundary-layer recirculation is determined. The graph of w_{BL} is fitted to the profile found in DNS over the range $R - \delta_{S,1/4} \leqslant r \leqslant R$, the sidewall boundary layer, using a least-squares approach. The result of this fit is $C = -0.032$. The value of C is rather small; note that velocity is scaled with $U = \sqrt{g\alpha\Delta T H}$, which is the maximal velocity that could occur in this flow. The mean

Symbol	Equation	Where?	Corrected by side	Corrected by b/t	Order in E velocity	Order in E flux
$\tilde{u}_{(0)}$	(2.11*a*)	5 ($\delta_{S,1/3}$)	0	0	$E^{1/3}$	$E^{1/3}$
$\tilde{v}_{(0)}$	(2.11*b*)	5 ($\delta_{S,1/3}$)	V	0	E^{0}	
$\tilde{w}_{(0)}$	(2.11*c*)	5 ($\delta_{S,1/3}$)	0	0	E^{0}	
$\tilde{u}_{(2)}$	(2.18*a*)	5 ($\delta_{S,1/3}$)	U	0	$E^{1/2}$	$E^{1/2}$
$\tilde{v}_{(2)}$	(2.18*b*)	5 ($\delta_{S,1/3}$)	0	0	$E^{1/6}$	
$\tilde{w}_{(2)}$	(2.18*c*)	5 ($\delta_{S,1/3}$)	0, corner	0	$E^{1/6}$	
U	(2.20*a*)	3 ($\delta_{S,1/4}$)	$\tilde{u}_{(2)}$	—	$E^{1/2}$	$E^{1/2}$
V	(2.20*b*)	3 ($\delta_{S,1/4}$)	$\tilde{v}_{(0)}$	V_E	E^{0}	
W	(2.20*c*)	3 ($\delta_{S,1/4}$)	$\tilde{w}_{(3)}$	W_E	$E^{1/4}$	
U_E	(2.21*a*)	4 ($\delta_E \cap \delta_{S,1/4}$)	corner	0	E^{0}	$E^{1/2}$
V_E	(2.21*b*)	4 ($\delta_E \cap \delta_{S,1/4}$)	corner	V	E^{0}	
W_E	(2.21*c*)	4 ($\delta_E \cap \delta_{S,1/4}$)	—	W	$E^{1/4}$	
$\tilde{u}_{(3)}$	(2.22*a*)	5 ($\delta_{S,1/3}$)	0	0	$E^{7/12}$	$E^{7/12}$
$\tilde{v}_{(3)}$	(2.22*b*)	5 ($\delta_{S,1/3}$)	0	0	$E^{1/4}$	
$\tilde{w}_{(3)}$	(2.22*c*)	5 ($\delta_{S,1/3}$)	W	0	$E^{1/4}$	
u_b	(A 3*b*)	1 (bulk)	$\bar{U}$	—	$E^{1/2}$	$E^{1/2}$
v_b	(A 1)	1 (bulk)	$\bar{V}$	v_E	E^{0}	
w_b	(A 3*a*)	1 (bulk)	—	w_E	$E^{1/2}$	
u_E	(A 2*a*)	2 (δ_E)	$\bar{U}_E$	0	E^{0}	$E^{1/2}$
v_E	(A 2*b*)	2 (δ_E)	$\bar{V}_E$	v_b	E^{0}	
w_E	(A 2*c*)	2 (δ_E)	—	w_b	$E^{1/2}$	
$\bar{U}$	(A 4*a*)	3 ($\delta_{S,1/4}$)	u_b	—	$E^{1/2}$	$E^{1/2}$
$\bar{V}$	(A 4*b*)	3 ($\delta_{S,1/4}$)	v_b	$\bar{V}_E$	E^{0}	
$\bar{W}$	(A 4*c*)	3 ($\delta_{S,1/4}$)	$\tilde{\bar{w}}_{(3)}$	$\bar{W}_E$	$E^{1/4}$	
$\bar{U}_E$	(A 5*a*)	4 ($\delta_E \cap \delta_{S,1/4}$)	u_E	0	E^{0}	$E^{1/2}$
$\bar{V}_E$	(A 5*b*)	4 ($\delta_E \cap \delta_{S,1/4}$)	v_E	$\bar{V}$	E^{0}	
$\bar{W}_E$	(A 5*c*)	4 ($\delta_E \cap \delta_{S,1/4}$)	—	$\bar{W}$	$E^{1/4}$	
$\tilde{\bar{u}}_{(3)}$	$-\frac{C'R}{C} \times$ (2.22*a*)	5 ($\delta_{S,1/3}$)	0	0	$E^{7/12}$	$E^{7/12}$
$\tilde{\bar{v}}_{(3)}$	$-\frac{C'R}{C} \times$ (2.22*b*)	5 ($\delta_{S,1/3}$)	0	0	$E^{1/4}$	
$\tilde{\bar{w}}_{(3)}$	$-\frac{C'R}{C} \times$ (2.22*c*)	5 ($\delta_{S,1/3}$)	$\bar{W}$	0	$E^{1/4}$	

TABLE 1. Summary of the velocity fields. The symbols used in this work are mentioned along with the equation number of the final result for each contribution. The location of its primary contribution (bulk or a specific boundary layer) is also noted for each velocity. We also include the fields that, when necessary, correct this velocity to zero on the sidewall ('side') or on the bottom and top ('b/t'); a 0 indicates that this contribution is zero on that boundary. The entry 'corner' designates the correction due to the corner regions at the sidewall. Finally, the orders of magnitude in E are given for the velocity components as well as the associated fluxes.

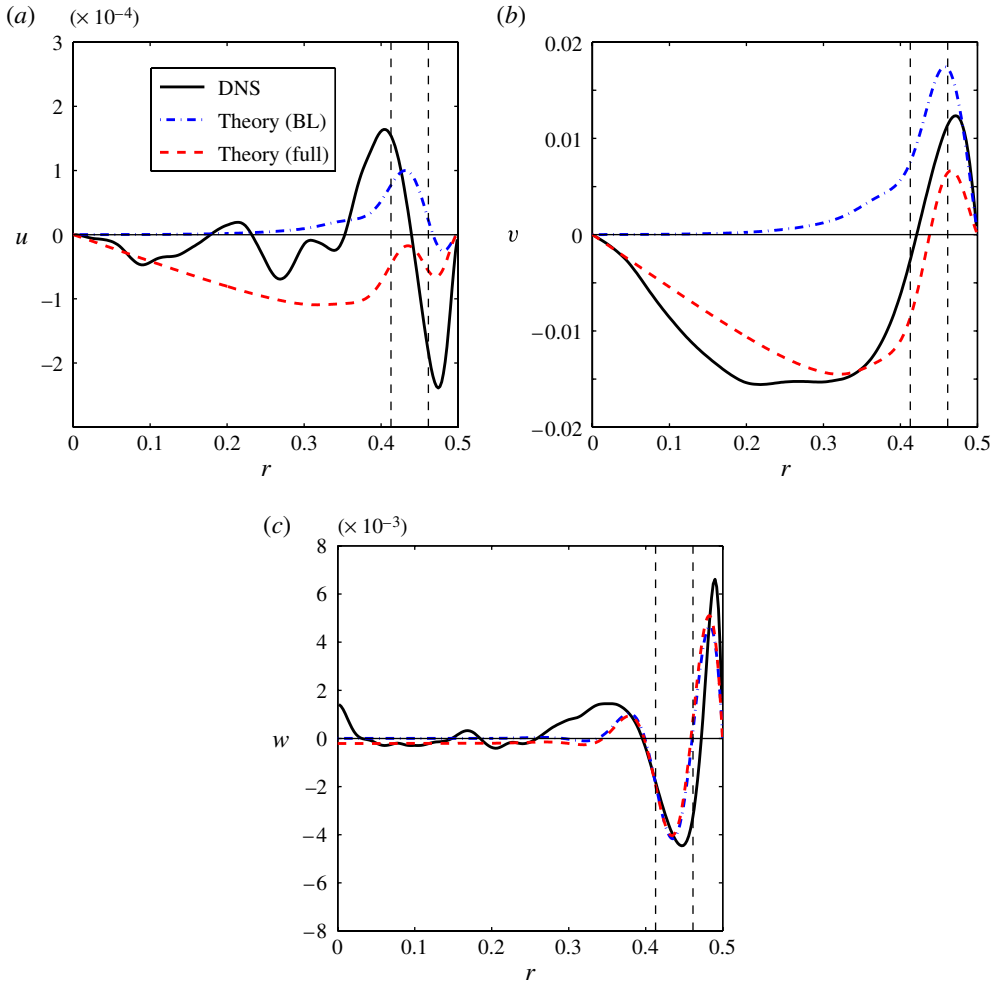

FIGURE 5. (Colour online) Comparison between DNS and theory of velocity profiles at level $z = -0.25$ in radial direction: (*a*) radial velocity u; (*b*) azimuthal velocity v; (*c*) vertical velocity w. In each panel, the solid black line indicates the mean velocity component from DNS. The dashed line (red online) is the full theoretical model fitted to the DNS results. The dash-dotted line (blue online) depicts the interim result of the boundary-layer circulation fitted to the w component of the DNS result. The vertical dashed lines represent the theoretical boundary layer thicknesses $\delta_{S,1/3} = E^{1/3}$ (closest to the sidewall) and $\delta_{S,1/4} = E^{1/4}$.

circulation discussed here is small in amplitude compared with the turbulent velocity fluctuations. In figure 5 we compare the radial profiles of u, v and w at $z = -0.25$ from DNS (black solid lines) with the boundary-layer recirculation at this amplitude C (dash-dotted lines; blue online). For the vertical velocity w, a satisfactory agreement is reached; however, especially for the azimuthal velocity v, there is a clear additional contribution due to the bulk circulation.

As a second step, the amplitude C' of the bulk circulation, which is introduced in appendix A, is to be quantified. Given that the azimuthal velocity v is of lowest order

in E, it is best suited for the actual fitting. We fit the sum $v_{bulk} = v_b + \bar{V} + \bar{\tilde{v}}_{(3)}E^{1/4}$, defined in appendix A, to the remainder of the corresponding DNS profile after subtraction of the contribution of the boundary-layer recirculation, again using a least-squares procedure, but this time covering the full radial extent $0 \leqslant r \leqslant R$. The resulting amplitude is $C' = -0.055$. The final results from this procedure (sum of boundary-layer and bulk circulations) are included in figure 5 with dashed lines (red online).

It is found that the theory captures all of the features of the profiles from the DNS. However, the exact relative amplitudes and locations of the maxima and minima can be slightly off. This is, of course, not surprising given the stringent assumptions and simplifications of the model. The excellent agreement of the azimuthal and vertical velocities, in particular, even at this large Rossby number $Ro = 0.72$, is practically a validation of these assumptions, which appear to have validity even for non-vanishing Ro. It is to be expected that nonlinear effects and, to a lesser degree, curvature effects, present in the DNS but not in the theoretical model, must have some effects on the DNS profiles, so that they cannot be fully covered by the model. The radial velocity does not reveal as good a match. In an absolute sense, the radial velocity component reaches much smaller values than the other components, making it more susceptible to effects of turbulent fluctuations that may complicate the convergence of the mean. Nevertheless, we want to emphasize the success of a time-independent, linearized, axisymmetric model to represent mean velocity profiles of a vigorously turbulent flow.

As an additional comparison, the full velocity fields obtained from the linear analysis are presented in figure 6. These show the bottom half of the domain for comparison with figures 1 and 2. Most of the structures found in the DNS results are also represented in the theoretical result. However, one major deviation is noticeable in the azimuthal velocity component v. In the model, the largest positive velocity is found in the corner region; whereas, in the DNS, the maximum is found at midheight $z = 0$, near the sidewall. This is primarily an artifact of the delta-function approximation used in the $E^{1/3}$ layer. By explicitly prescribing such discontinuous stepwise changes in the flow field – which actually cover a small but finite distance in reality – unphysically large velocity gradients occur near the corner region, which in turn produce unphysical flow structures. The mathematical simplification of the delta function, while mathematically sound and *essential* to arrive at the solution, unavoidably leads to these artifacts. Additionally, the flow in the corner region of dimensions $E^{1/2} \times E^{1/2}$ is missing from these visualizations. The velocity contributions in this corner region, which rapidly drop off outside, should compensate some non-zero velocity contributions on the walls (see table 1). However, given that analytical solutions are not readily found and their range of influence is very limited, we do not consider these contributions here. Nevertheless, in spite of these shortcomings, the solutions found here describe the mean flow quite accurately for most of the domain.

3.2. *Dependence on the Ekman number*

The bulk flow pattern changes when lower Ekman numbers $E = (0.72, 1.44, 2.88) \times 10^{-5}$ are considered. The bulk circulation as introduced previously is suppressed. Since we are interested in the sidewall boundary layers, we focus on the velocity field near the sidewall, which shows the same boundary-layer signature for all considered Ekman numbers. In figure 7 we compare the mean vertical velocity w near the sidewall at height $z = -0.4$ from DNS with our theoretical model result for the boundary-layer recirculation. Owing to the mismatch of the peak positions, especially at the lowest E

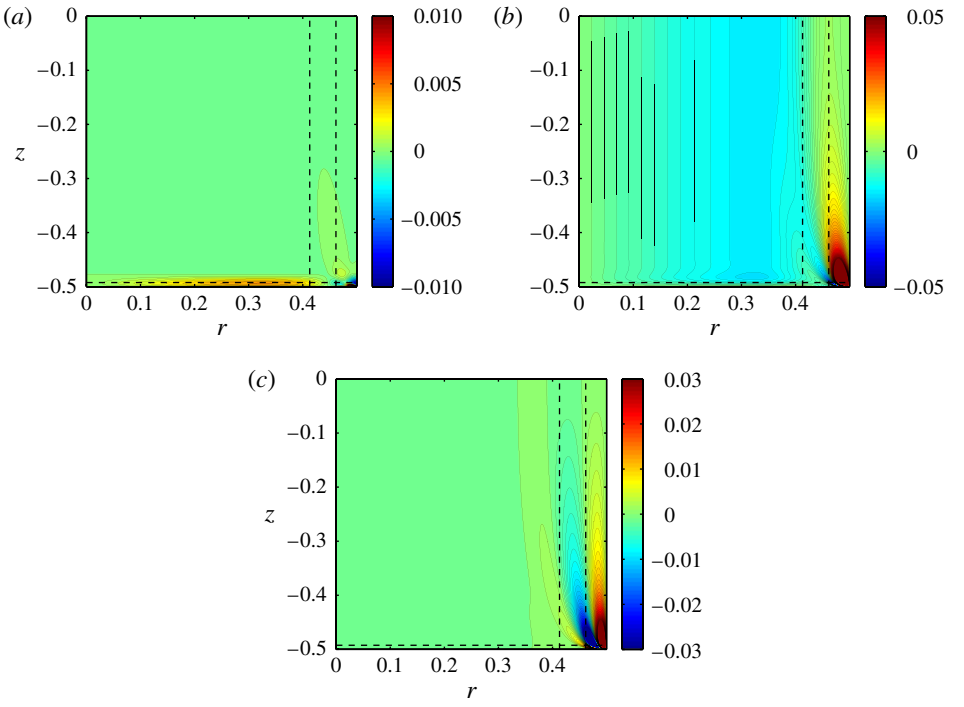

FIGURE 6. The sum total of the velocity fields obtained from linear boundary-layer analysis with $E = 5.76 \times 10^{-5}$ with amplitudes as fitted to the DNS results of figures 1 and 2: shown are (*a*) u, (*b*) v and (*c*) w. The dashed lines represent the characteristic boundary-layer thicknesses $\delta_E = E^{1/2}$ (close to the bottom), $\delta_{S,1/3} = E^{1/3}$ (vertical line closest to the right-hand side), and $\delta_{S,1/4} = E^{1/4}$ (leftmost vertical line).

values, a direct least-squares procedure is not suitable. Instead, we choose C such that the peak value of w closest to the sidewall is the same for both DNS and theory. In figure 7(*e*) the absolute value of the strength $|C|$ of the boundary-layer recirculation (C is negative in all cases) is plotted as a function of E. The shape of the boundary layer is nicely captured by the theory. There are different conditions in the bulk. In some cases the bulk region shows hardly any mean velocity (e.g. at $E = 2.88 \times 10^{-5}$), while in others there are well-defined up- and down-going parts (the two lowest Ekman numbers considered here). We speculate that, at the lower Ekman numbers, a steadier, more organized array of columnar vortices is found, which leave a distinct mark on the mean vertical velocity. We expect that only after very long averaging (too long for DNS) will the bulk have attained a mean velocity close to zero. When the mean velocity in the bulk is approximately zero, like for example at $E = 2.88 \times 10^{-5}$, the boundary-layer theory matches the DNS result to great detail. The amplitude C of the mean circulation varies quite a bit between the cases considered here with different values of E. This appears to be a reflection of the reduction of vertical velocity fluctuations in the bulk due to rotation. The four points seem to suggest a power-law behaviour: an appropriate slope would be $C \sim E^{1.8}$. Note that the theory presented in this paper cannot predict the amplitude C; we cannot explain this scaling from the current analysis.

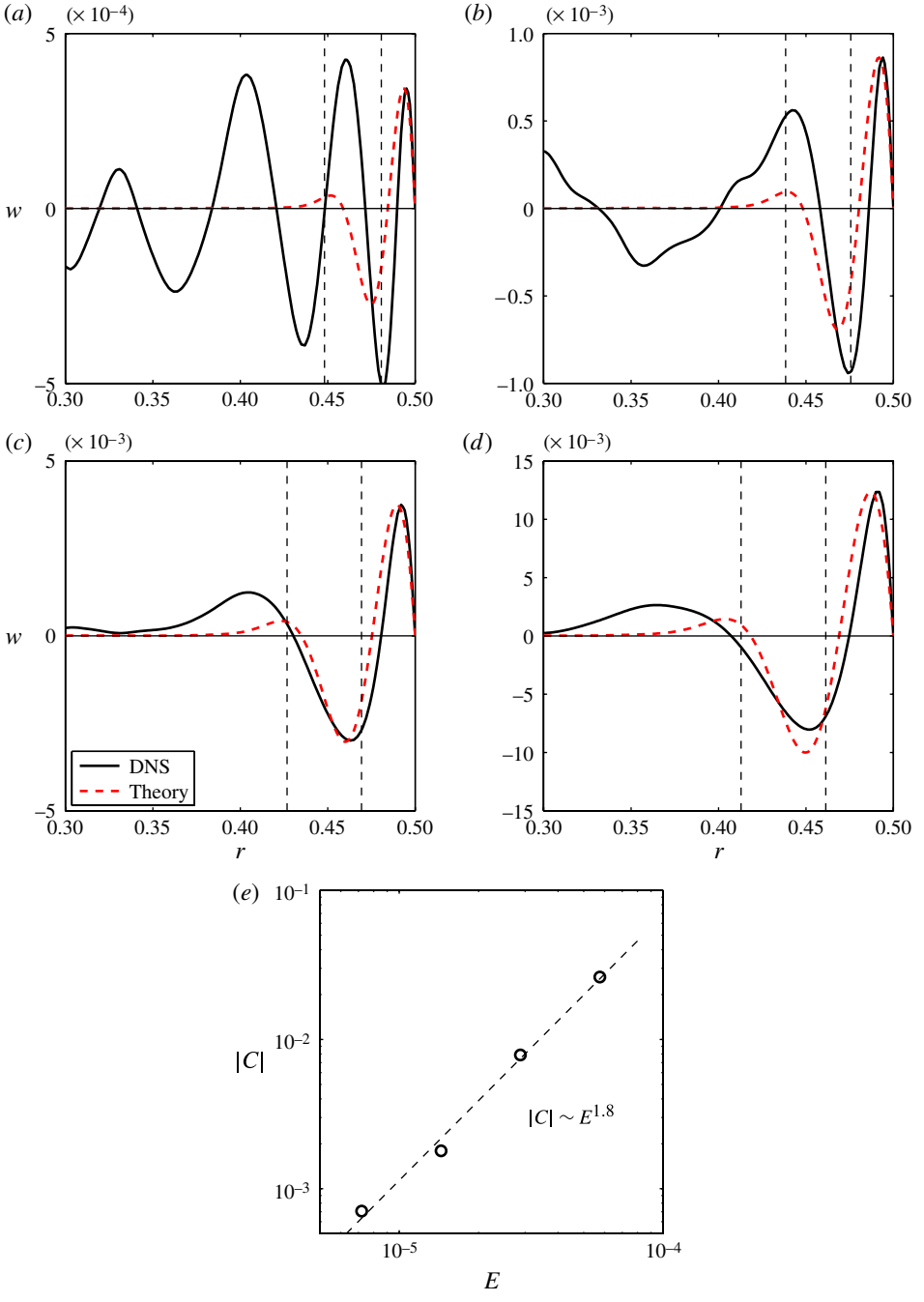

FIGURE 7. (Colour online) (*a–d*) Profiles of vertical velocity near the sidewall at height $z = -0.4$, from DNS (solid black lines) and theory (dashed lines, red online): (*a*) $E = 0.72 \times 10^{-5}$; (*b*) $E = 1.44 \times 10^{-5}$; (*c*) $E = 2.88 \times 10^{-5}$; (*d*) $E = 5.76 \times 10^{-5}$. The theoretical boundary-layer thicknesses are also included (vertical black dashed lines): $\delta_{S,1/3} = E^{1/3}$ (closest to the sidewall) and $\delta_{S,1/4} = E^{1/4}$. Note the differences in the scaling of the vertical axes. (*e*) Strength $|C|$ of the theoretical boundary-layer circulation as fitted to the DNS results as a function of E. A representative power-law fit is also included.

4. Conclusion

We have presented a theoretical linear boundary-layer analysis of rotating thermal convection in a cylindrical container. The sidewall boundary layer can be treated as a superposition of two independent parts: a bulk-driven circulation covering the entire cell, and a sidewall boundary-layer recirculation. Both parts have the structure typical of the Stewartson boundary layer, consisting of two sandwiched layers of typical thickness $\delta_{S,1/4}$ and $\delta_{S,1/3}$. The linear model has a surprisingly good agreement with the temporally and azimuthally averaged velocity from DNS runs of turbulent rotating convection in a cylinder. It is found that the bulk-driven part is not always the same, which may be due to long-time dynamics of the array of columnar vortices in the bulk that makes it impossible in practice to average them out with DNS. This is especially true for the lowest Ekman numbers $E \lesssim 2 \times 10^{-5}$ considered here. The boundary-layer part, however, can be observed throughout the considered Ekman number range.

Possible extensions to the current results include the addition of curvature terms in the sidewall boundary layers. As a result, the exponential functions containing the boundary-layer coordinates ξ or η would be replaced with Bessel functions, making the analysis considerably more difficult. Another consideration is to include the coupling of the $E^{1/3}$ layer with the Ekman layers on top and bottom, which allows more wavelengths in the harmonic terms governing the vertical dependence. The results will surely be more convoluted and may even not allow for analytical descriptions.

The linear description of boundary layers has been very successful in non-rotating turbulent convection, with the theory of Grossmann and Lohse (Ahlers, Grossmann & Lohse 2009) as a most remarkable result, predicting the heat transfer (Nusselt number) and large-scale flow strength (Reynolds number) as functions of the input parameters Ra and σ. The current linear boundary-layer description may serve as a starting point to extend the theory to the rotating frame. It is highly remarkable how linear theories can still produce valuable results even in vigorously turbulent flow.

Acknowledgements

We gratefully acknowledge discussions with R. Stevens on this topic. We thank R. Verzicco for providing the numerical code. R.P.J.K. wishes to thank the Foundation for Fundamental Research on Matter (Stichting voor Fundamenteel Onderzoek der Materie, FOM) for financial support. This work was sponsored by the National Computing Facilities Foundation (NCF) for the use of supercomputer facilities (Huygens), with financial support from the Netherlands Organization for Scientific Research (NWO).

Appendix A. The 'spin-up' circulation

In figure 1 a bulk-driven secondary circulation can be observed, which bears a resemblance to the classical problem of spin-up. The spin-up process in a closed cylinder is a topic that has received much attention (see e.g. Greenspan & Howard 1963; Benton & Clark 1974; Duck & Foster 2001, and references therein). We start by observing that, in the bulk, close to the cylinder axis, the azimuthal bulk velocity v_b is a linear function of the radial coordinate,

$$v_b = -C'r, \tag{A 1}$$

with C' a positive constant. This situation is analogous to instantaneous spin-up, only now the problem is independent of time. In the bulk (region **1** in figure 3), the dominant force equilibrium is thus the geostrophic balance of pressure gradient and

Coriolis force, so that we can immediately conclude that the radial velocity u_b and vertical velocity w_b in the bulk are zero to leading order E^0.

It is obvious that this flow does not connect to the boundaries. The bulk flow is connected to the bottom and top plates at $z = \pm 1/2$ by Ekman boundary layers (region **2** in figure 3) of thickness $\delta_E = E^{1/2}$. Focusing on the bottom plate, in terms of the scaled boundary-layer coordinate $\zeta = (z + 1/2)E^{-1/2}$, the standard Ekman-layer solutions are

$$u_E = -v_b \sin\zeta\, \mathrm{e}^{-\zeta} = C' r \sin\zeta\, \mathrm{e}^{-\zeta}, \tag{A 2a}$$

$$v_E = -v_b \cos\zeta\, \mathrm{e}^{-\zeta} = C' r \cos\zeta\, \mathrm{e}^{-\zeta}, \tag{A 2b}$$

where u_E and v_E are *corrections* to the bulk field, so that the sums $u = u_b + u_E$ and $v = v_b + v_E$ are zero to leading order E^0 on the plates at $z = \pm 1/2$. From continuity, it follows immediately that

$$w_E = C'(\cos\zeta + \sin\zeta)\mathrm{e}^{-\zeta} E^{1/2}, \tag{A 2c}$$

which, as a boundary-layer correction, must vanish for $\zeta \to \infty$. To meet the boundary conditions on the plates, the sum $w = w_b + w_E$ must be zero there, meaning that there is an $O(E^{1/2})$ vertical velocity w_b in the bulk. The boundary conditions for w are met to order $E^{1/2}$. Because of the vertical symmetry, the proposed contribution is

$$w_b = 2C' z E^{1/2}, \tag{A 3a}$$

with a radial contribution u_b that is found from incompressibility,

$$u_b = -C' r E^{1/2}. \tag{A 3b}$$

There is a net radially outward flux due to u_E in the Ekman layers and an equally large radially inward flux through the bulk due to u_b. This circulation must be closed with a nested pair of Stewartson layers.

The Stewartson layer (region **3** in figure 3) must carry an $O(E^{1/2})$ vertical flux to close the circulation from the outward radial fluxes in the Ekman layers to the radial inward flux through the bulk. From the equations in the boundary-layer approximation for the sidewall with neglect of curvature terms, it can be concluded that a layer of characteristic thickness $E^{1/4}$ is required. It delivers a contribution $\bar{U}$ of $O(E^{1/2})$ to the radial velocity, $\bar{V}$ of $O(E^0)$ to the azimuthal velocity, and $\bar{W}$ of $O(E^{1/4})$ vertically (e.g. Greenspan & Howard 1963; van Heijst 1986). By application of the boundary conditions $u_b(r = R) + \bar{U}(r = R) = 0$ and $v_b(r = R) + \bar{V}(r = R) = 0$, we arrive at the following solutions, expressed as functions of the boundary-layer coordinate $\xi = (r - R)E^{-1/4}$:

$$\bar{U} = C' R \exp(\sqrt{2}\xi) E^{1/2}, \tag{A 4a}$$

$$\bar{V} = C' R \exp(\sqrt{2}\xi), \tag{A 4b}$$

$$\bar{W} = -\sqrt{2} C' R z \exp(\sqrt{2}\xi) E^{1/4}. \tag{A 4c}$$

Close to the bottom and top plates, the dynamics remains governed by the Ekman-layer dynamics. The following Ekman-layer corrections occur in region **5** of figure 3:

$$\bar{U}_E = -C' R \exp(\sqrt{2}\xi) \sin\zeta\, \mathrm{e}^{-\zeta}, \tag{A 5a}$$

$$\bar{V}_E = -C' R \exp(\sqrt{2}\xi) \cos\zeta\, \mathrm{e}^{-\zeta}, \tag{A 5b}$$

$$\bar{W}_E = -\tfrac{1}{2}\sqrt{2} C' R \exp(\sqrt{2}\xi)(\sin\zeta + \cos\zeta)\mathrm{e}^{-\zeta} E^{1/4}. \tag{A 5c}$$

These corrections take care of the bottom/top boundary conditions to leading order in E, such that $\bar{U} + \bar{U}_E(\zeta = 0) = 0$, $\bar{V} + \bar{V}_E(\zeta = 0) = 0$ and $\bar{W}(z = -1/2) + \bar{W}_E(\zeta = 0) = 0$. Also, on the sidewall, we find that $u_E(r = R) + \bar{U}_E(\xi = 0) = 0$ and $v_E(r = R) + \bar{V}_E(\xi = 0) = 0$. All of the leading-order velocities correctly match with the boundary conditions except for $\bar{W}$ on the sidewall, which requires an additional sidewall boundary layer, this time of thickness $E^{1/3}$ (Greenspan & Howard 1963).

The Stewartson $E^{1/3}$ layer (region **6** of figure 3) is typically described by a series expansion of the form (2.4). For the current purpose of correcting $W \sim O(E^{1/4})$ on the sidewall, it is clear that the $k = 3$ field from the series expansion is required. The functional forms, which we shall not repeat here, are the set (2.21) multiplied by $-C'R/C$.

The sum of the velocity fields in this appendix is a closed circulation, analogous to the spin-up problem, that satisfies all boundary conditions to leading order.

Appendix B. Convergence and numerical evaluation of the series expansions

The series solutions obtained in this paper are non-trivial to evaluate numerically. Their convergence can be very slow. That they do converge can be proved as follows. The basic structure of the series is

$$f(\eta, z) \sim \sum_{n=1}^{\infty} (-1)^n \gamma_n^k \sin(2\pi n z) \mathrm{e}^{\gamma_n \eta}, \tag{B 1}$$

where $\gamma_n = (2\pi n)^{1/3}$, the sine may be replaced by a cosine, and several values of k may arise, *viz.* $k = -2, -1, 0, 2$. Note that $\eta \leqslant 0$ by definition.

For $k = -2$, -1 or 0, it is true that

$$|(-1)^n \gamma_n^k \sin(2\pi n z) \mathrm{e}^{\gamma_n \eta}| \leqslant \mathrm{e}^{\gamma_n \eta}. \tag{B 2}$$

This also covers factors $1/n$ as in (2.22*b*). Such series can be treated with the integral test. Let

$$a_n = g(n) = \exp((2\pi n)^{1/3} \eta) \tag{B 3}$$

with $\eta < 0$. The series $\sum_{n=1}^{\infty} a_n$ converges when the integral $\int_1^{\infty} g(n)\,\mathrm{d}n$ is finite. We find that

$$\begin{aligned} \int_1^{\infty} g(n)\,\mathrm{d}n &= \int_1^{\infty} \exp[(2\pi n)^{1/3} \eta]\,\mathrm{d}n \\ &= -\frac{3\exp[(2\pi)^{1/3}\eta]}{2\pi\eta^3}[2 + (2\pi)^{1/3}\eta((2\pi)^{1/3}\eta - 2)], \end{aligned} \tag{B 4}$$

which indeed is finite, so the series is convergent for $\eta < 0$.

The case $k = 2$ can be handled in a similar fashion. For $\eta < 0$, it is always true that

$$|(-1)^n \gamma_n^2 \sin(2\pi n z) \mathrm{e}^{\gamma_n \eta}| \leqslant \gamma_n^2 \mathrm{e}^{\gamma_n \eta}, \tag{B 5}$$

which is to be treated with the integral test. Let

$$a_n = g(n) = (2\pi n)^{2/3} \exp((2\pi n)^{1/3} \eta). \tag{B 6}$$

The integral

$$\int_1^\infty g(n)\,\mathrm{d}n = \int_1^\infty (2\pi n)^{2/3}\exp[(2\pi n)^{1/3}\eta]\,\mathrm{d}n$$
$$= -\frac{3\exp[(2\pi)^{1/3}\eta]}{\pi\eta^5}[12 - 12(2\pi)^{1/3}\eta + 6(2\pi)^{2/3}\eta^2 - 4\pi\eta^3 + \pi(2\pi)^{1/3}\eta^4] \tag{B 7}$$

is still finite, so the series converges. The factor $1/2$ in the exponent, as found in (2.18) for example, does not cause the series to diverge.

For all $\eta < 0$, the series representations of the velocity fields are convergent. For $\eta = 0$, the series coefficients are either zero or the series are matched with the known Fourier series (2.8) or (2.23). So all series representations are convergent for all $\eta \leqslant 0$. However, there are discontinuities in the 'corner' points $\eta = 0$ and $z = \pm 1/2$, which, of course, can never match physically realistic flows.

For the numerical evaluation of the series, it is not practicable to simply sum the first N terms, given their slow convergence. Here Cesàro summation is applied. Let

$$S_k = \sum_{n=1}^{k} a_n \tag{B 8}$$

be the kth partial sum of the series $\{s_n\} = \sum_{n=1}^{\infty} a_n$. The series $\{s_n\}$ is Cesàro summable with Cesàro sum A when the limit

$$\lim_{n\to\infty} \frac{1}{n}\sum_{k=1}^{n} S_k = A \tag{B 9}$$

exists. The truncated Cesàro summation converges more rapidly than a truncated sum of the original series.

REFERENCES

AHLERS, G., GROSSMANN, S. & LOHSE, D. 2009 Heat transfer and large scale dynamics in turbulent Rayleigh–Bénard convection. *Rev. Mod. Phys.* **81**, 503–537.

BARCILON, V. & PEDLOSKY, J. 1967*a* Linear theory of rotating stratified fluid flows. *J. Fluid Mech.* **29**, 1–16.

BARCILON, V. & PEDLOSKY, J. 1967*b* A unified linear theory of homogeneous and stratified rotating fluids. *J. Fluid Mech.* **29**, 609–621.

BENTON, E. R. & CLARK, A. 1974 Spin-up. *Annu. Rev. Fluid Mech.* **6**, 257–280.

CHANDRASEKHAR, S. 1961 *Hydrodynamic and Hydromagnetic Stability*. Oxford University Press.

DUCK, P. W. & FOSTER, M. R. 2001 Spin-up of homogeneous and stratified fluids. *Annu. Rev. Fluid Mech.* **33**, 231–263.

ECKE, R. E. & LIU, Y. 1998 Traveling-wave and vortex states in rotating Rayleigh–Bénard convection. *Intl J. Engng Sci.* **36**, 1471–1480.

GREENSPAN, H. P. 1968 *The Theory of Rotating Fluids*. Cambridge University Press.

GREENSPAN, H. P. & HOWARD, L. N. 1963 On a time-dependent motion of a rotating fluid. *J. Fluid Mech.* **17**, 385–404.

HART, J. E., KITTELMAN, S. & OHLSEN, D. R. 2002 Mean flow precession and temperature probability density functions in turbulent rotating convection. *Phys. Fluids* **14**, 955–962.

HART, J. E. & OHLSEN, D. R. 1999 On the thermal offset in turbulent rotating convection. *Phys. Fluids* **11**, 2101–2107.

VAN HEIJST, G. J. F. 1983 The shear-layer structure in a rotating fluid near a differentially rotating sidewall. *J. Fluid Mech.* **130**, 1–12.

VAN HEIJST, G. J. F. 1986 Fluid flow in a partially-filled rotating cylinder. *J. Engng Maths* **20**, 233–250.

KUNNEN, R. P. J., CLERCX, H. J. H. & GEURTS, B. J. 2008*a* Breakdown of large-scale circulation in turbulent rotating convection. *Europhys. Lett.* **84**, 24001.

KUNNEN, R. P. J., CLERCX, H. J. H. & GEURTS, B. J. 2008*b* Enhanced vertical inhomogeneity in turbulent rotating convection. *Phys. Rev. Lett.* **101**, 174501.

KUNNEN, R. P. J., GEURTS, B. J. & CLERCX, H. J. H. 2010*a* Experimental and numerical investigation of turbulent rotating convection. *J. Fluid Mech.* **642**, 445–476.

KUNNEN, R. P. J., GEURTS, B. J. & CLERCX, H. J. H. 2010*b* Vortex statistics in turbulent rotating convection. *Phys. Rev.* E **80**, 036314.

KUNNEN, R. P. J., STEVENS, R. J. A. M., OVERKAMP, J., SUN, C., VAN HEIJST, G. J. F. & CLERCX, H. J. H. 2011 The role of Stewartson and Ekman layers in turbulent rotating Rayleigh–Bénard convection. *J. Fluid Mech.* **688**, 422–442.

LIGHTHILL, M. J. 1968 *Introduction to Fourier Analysis and Generalized Functions*. Cambridge University Press.

MARSHALL, J. & SCHOTT, F. 1999 Open-ocean convection: observations, theory, and models. *Rev. Geophys.* **37**, 1–64.

MIESCH, M. S. 2000 The coupling of solar convection and rotation. *Solar Phys.* **192**, 59–89.

MOORE, D. W. & SAFFMAN, P. G. 1969 The structure of free vertical shear layers in a rotating fluid and the motion produced by a slowly rising body. *Phil. Trans. R. Soc.* A **264**, 597–634.

NIEMELA, J. J., BABUIN, S. & SREENIVASAN, K. R. 2010 Turbulent rotating convection at high Rayleigh and Taylor numbers. *J. Fluid Mech.* **649**, 509–522.

PROUDMAN, I. 1956 The almost-rigid rotation of viscous flow between concentric spheres. *J. Fluid Mech.* **1**, 505–516.

ROSSBY, H. T. 1969 A study of Bénard convection with and without rotation. *J. Fluid Mech.* **36**, 309–335.

VAN SANTEN, H., KLEIJN, C. R. & VAN DEN AKKER, H. E. A. 2000 On turbulent flows in cold-wall CVD reactors. *J. Cryst. Growth* **212**, 299–310.

STEVENS, R. J. A. M., CLERCX, H. J. H. & LOHSE, D. 2010 Optimal Prandtl number for heat transfer in rotating Rayleigh–Bénard convection. *New J. Phys.* **12**, 075005.

STEVENS, R. J. A. M., CLERCX, H. J. H. & LOHSE, D. 2012 Breakdown of the large-scale circulation in $\gamma = 1/2$ rotating Rayleigh–Bénard flow. *Phys. Rev.* E **86**, 056311.

STEVENS, R. J. A. M., OVERKAMP, J., LOHSE, D. & CLERCX, H. J. H. 2011 Effect of aspect ratio on vortex distribution and heat transfer in rotating Rayleigh–Bénard convection. *Phys. Rev.* E **84**, 056313.

STEWARTSON, K. 1957 On almost rigid rotations. *J. Fluid Mech.* **3**, 17–26.

VOROBIEFF, P. & ECKE, R. E. 1998*a* Transient states during spin-up of a Rayleigh–Bénard cell. *Phys. Fluids* **10**, 2525–2538.

VOROBIEFF, P. & ECKE, R. E. 1998*b* Vortex structure in rotating Rayleigh–Bénard convection. *Physica* D **123**, 153–160.

VOROBIEFF, P. & ECKE, R. E. 2002 Turbulent rotating convection: an experimental study. *J. Fluid Mech.* **458**, 191–218.

WEISS, S. & AHLERS, G. 2011*a* Heat transport by turbulent rotating Rayleigh–Bénard convection and its dependence on the aspect ratio. *J. Fluid Mech.* **684**, 407–426.

WEISS, S. & AHLERS, G. 2011*b* The large-scale flow structure in turbulent rotating Rayleigh–Bénard convection. *J. Fluid Mech.* **688**, 461–492.

WEISS, S., STEVENS, R. J. A. M., ZHONG, J.-Q., CLERCX, H. J. H., LOHSE, D. & AHLERS, G. 2010 Finite-size effects lead to supercritical bifurcations in turbulent rotating Rayleigh–Bénard convection. *Phys. Rev. Lett.* **105**, 224501.

ZHONG, F., ECKE, R. E. & STEINBERG, V. 1991 Asymmetric modes and the transition to vortex structures in rotating Rayleigh–Bénard convection. *Phys. Rev. Lett.* **67**, 2473–2476.

ZHONG, F., ECKE, R. E. & STEINBERG, V. 1993 Rotating Rayleigh–Bénard convection: asymmetric modes and vortex states. *J. Fluid Mech.* **249**, 135–159.

ZHONG, J.-Q. & AHLERS, G. 2010 Heat transport and the large-scale circulation in rotating turbulent Rayleigh–Bénard convection. *J. Fluid Mech.* **665**, 300–333.

ZHONG, J.-Q., STEVENS, R. J. A. M., CLERCX, H. J. H., VERZICCO, R., LOHSE, D. & AHLERS, G. 2009 Prandtl-, Rayleigh-, and Rossby-number dependence of heat transport in turbulent rotating Rayleigh–Bénard convection. *Phys. Rev. Lett.* **102**, 044502.